Bioorganic Chemistry 165 (2025) 109024

Contents lists available at ScienceDirect

Bioorganic Chemistry

journal homepage: www.elsevier.com/locate/bioorg

# Crystallographic fragment screening reveals new starting points for PYCR1 inhibitor design

Wiktoria Ragin-Oh [a], Dominika Czerwonka [a], Linh H. Tran [a], Giuseppe Forlani [b], Milosz Ruszkowski [a,*]

[a] Department of Structural Biology of Eukaryotes, Institute of Bioorganic Chemistry, Polish Academy of Sciences, Noskowskiego 12/14, 61-704 Poznan, Poland
[b] Department of Life Science and Biotechnology, University of Ferrara, Via L. Borsari, 46, 44121 Ferrara, FE, Italy

ARTICLE INFO

*Keywords:*
Pyrroline-5-carboxylate reductase 1 (PYCR1)
Proline metabolism
Metabolic reprogramming in cancer
Crystallographic fragment screening
Structure-based inhibitor design

ABSTRACT

Pyrroline-5-carboxylate (P5C) reductase catalyzes the final step in proline biosynthesis. Human P5C reductase isoform 1 (PYCR1) has emerged as a key metabolic enzyme supporting cancer progression through its roles in redox homeostasis, collagen production, and the proline-P5C cycle. Despite its relevance as a therapeutic target, structural and chemical efforts to inhibit PYCR1 remain limited and have largely focused on proline analogs. Here, we report the first crystallographic fragment screening (XFS) campaign against PYCR1, employing a chemically diverse library of 96 compounds. We solved twelve co-crystal structures, featuring ligands occupying the P5C and NADH binding pockets, including dual-site ligands that span both regions. Among the newly identified moieties, sulfonamide and sulfamate groups emerged as notable isosteric replacements for the carboxylate group in the PYCR1 active site. Aromatic substituents in several compounds revealed a cryptic subpocket near the nicotinamide-binding site. Interestingly, halogen-substituted aromatic rings, often present in known PYCR1 inhibitors, exhibited distinct binding orientations, reflecting the flexibility and diversity of interactions in the binding subpockets. High-resolution structures revealed ligand-induced conformational changes in PYCR1, some involving significant rearrangements. Molecular dynamics simulations indicated that these conformations are accessible in the ligand-free enzyme, underscoring the intrinsic plasticity of PYCR1's active site.

## 1. Introduction

Proline biosynthesis in mammals proceeds *via* two distinct pathways originating from either glutamate in the mitochondria or ornithine in the cytosol. Both pathways converge at the formation of $\Delta^1$-pyrroline-5-carboxylate (P5C), which is then reduced to proline by $\Delta^1$-pyrroline-5-carboxylate reductase (PYCR), utilizing equimolar amounts of NADH or NADPH as a cofactor. Among the PYCR isozymes, PYCR1 is the predominant form in human cells, underscoring its crucial role in proline production [1,2]. However, the function of PYCR1 in cellular physiology extends well beyond the synthesis of this proteinogenic amino acid. Recent years have produced accumulating evidence implicating PYCR1 in cancer progression. Elevated *PYCR1* expression has been observed across a wide range of malignancies, including highly aggressive types such as hepatocellular carcinoma [3–6], breast carcinoma [7–9], prostate cancer [10,11], and malignant melanoma [12]. Additionally, *PYCR1* overexpression correlates with advanced tumor stage and is associated with a poor prognosis [6,7,13–15], whereas *PYCR1* knockdown inhibits proliferation [3,9,10,16,17].

The molecular mechanism underlying the role of PYCR1 in tumorigenesis and cancer progression remains elusive. One prominent hypothesis involves the reprogramming of proline metabolism, which becomes profoundly altered in cancer cells to meet the demands of uncontrolled growth and metabolic stress [1,2,5,6,17,18]. Furthermore, proline has been identified as a restrictive amino acid in certain cancer types, including clear cell renal cell carcinoma and invasive ductal breast carcinoma [19]. Beyond its metabolic role, proline also contributes to cancer progression through its involvement in the biosynthesis of collagen, a key structural component of the extracellular matrix (ECM). Dysregulation of proline metabolism has been shown to affect ECM composition and dynamics, thereby enhancing the invasive potential of cancer cells and promoting metastatic spread [2,20,21].

An equally compelling hypothesis suggests that PYCR1 contributes to cancer progression through its role in maintaining redox homeostasis

* Corresponding author.
*E-mail address:* mruszkowski@ibch.poznan.pl (M. Ruszkowski).

https://doi.org/10.1016/j.bioorg.2025.109024
Received 5 August 2025; Received in revised form 15 September 2025; Accepted 22 September 2025
Available online 23 September 2025

and regenerating $NAD^+$ during proline biosynthesis. Under hypoxic conditions, when the mitochondrial electron transport chain is impaired, PYCR1 activity becomes a major source of $NAD^+$, thereby sustaining this essential metabolic processes [18,22,23]. This adaptive mechanism enables cancer cells to continue proliferating under stress conditions that would otherwise trigger apoptotic pathways. Recent studies have further expanded this concept by identifying a distinct subpopulation of mitochondria enriched in P5C synthetase (P5CS), which defines a specialized metabolic compartment [24]. These P5CS-positive mitochondria exhibit a proline-focused anabolic profile and have been shown to support redox balance and biosynthetic capacity. Strikingly, this form of mitochondrial specialization is prevalent in cancer cell lines but largely absent in non-transformed cells, highlighting its potential role in oncogenic metabolic remodeling [24].

A third possibility relies on the so-called proline-P5C cycle, a metabolic shortcut in which the P5C produced by proline dehydrogenase (ProDH), instead of being further oxidized to glutamate by P5C dehydrogenase, is reduced back to proline by PYCR1 in an apparently futile pathway. If the reductive half-cycle is catalyzed by the cytosol-localized PYCRL (also referred to as PYCR3), a net transfer of reducing equivalents from cytosolic NAD(*P*)H to the mitochondrial respiratory chain occurs as a consequence [25]. However, experimental evidence supporting a primary role of the mitochondrial PYCR isoforms 1 and 2 in the proline-P5C cycle has been described [26], leading to questions about the subcellular localization of PYCR1 [27]. In any case, the proline-P5C cycle has been shown to enhance oxidative phosphorylation and maintain pyridine nucleotide levels in the cytosol [28]. Moreover, the direct transfer of electrons from ProDH to the respiratory chain is susceptible to generating reactive oxygen species (ROS) that trigger various cell signaling cascades. ProDH-mediated ROS signaling can initiate apoptosis, inhibit tumor growth, block the cell cycle, and suppress hypoxia-inducible factor signaling. Consistently, *ProDH* was found to be under the control of the tumor suppressor protein p53 [29]. However, under metabolic stress such as oxygen and glucose deprivation, ProDH can, on the contrary, serve as a tumor survival factor through ATP production or ROS-induced autophagy [30]. Such a dual role of proline catabolism suggests a pro- or antisurvival effect in cancer cells depending on the context, and underlines that the ratio between proline synthesis and catabolism may play a major role in several cancer types [17].

Whatever the mechanism(s), the accumulating evidence supporting PYCR1's role in cancer progression and metastasis places it among the most promising targets for anticancer drug development. Nevertheless, since the connection between PYCR1 and cancer has been established recently, investigation of specific PYCR1 inhibitors remains at an early stage. A major limitation lies in the chemical space explored so far, which has been notably restricted due to reliance on highly focused compound libraries.

For instance, Tanner et al. conducted a preliminary screening by soaking PYCR1 crystals with proline mimics. In this study, *N*-formyl-L-proline (NFLP) emerged as the most potent inhibitor, exhibiting a $K_i$ of 99 μM (Fig. 1A) [31]. Building on this work, the same group later implemented a docking-guided, fragment-based screening of 37 carboxylic acid analogs. Within this expanded chemical space, compound 33 (Fig. 1A) surpassed NFLP in inhibitory potency [32]. In both reported studies, the authors prioritized P5C mimetics, a strategy that, while increasing hit rates within a defined framework, also restricts the diversity of scaffolds available for inhibitor design. Broader chemical screening efforts would offer better prospects for identifying novel scaffolds with greater inhibitory potency.

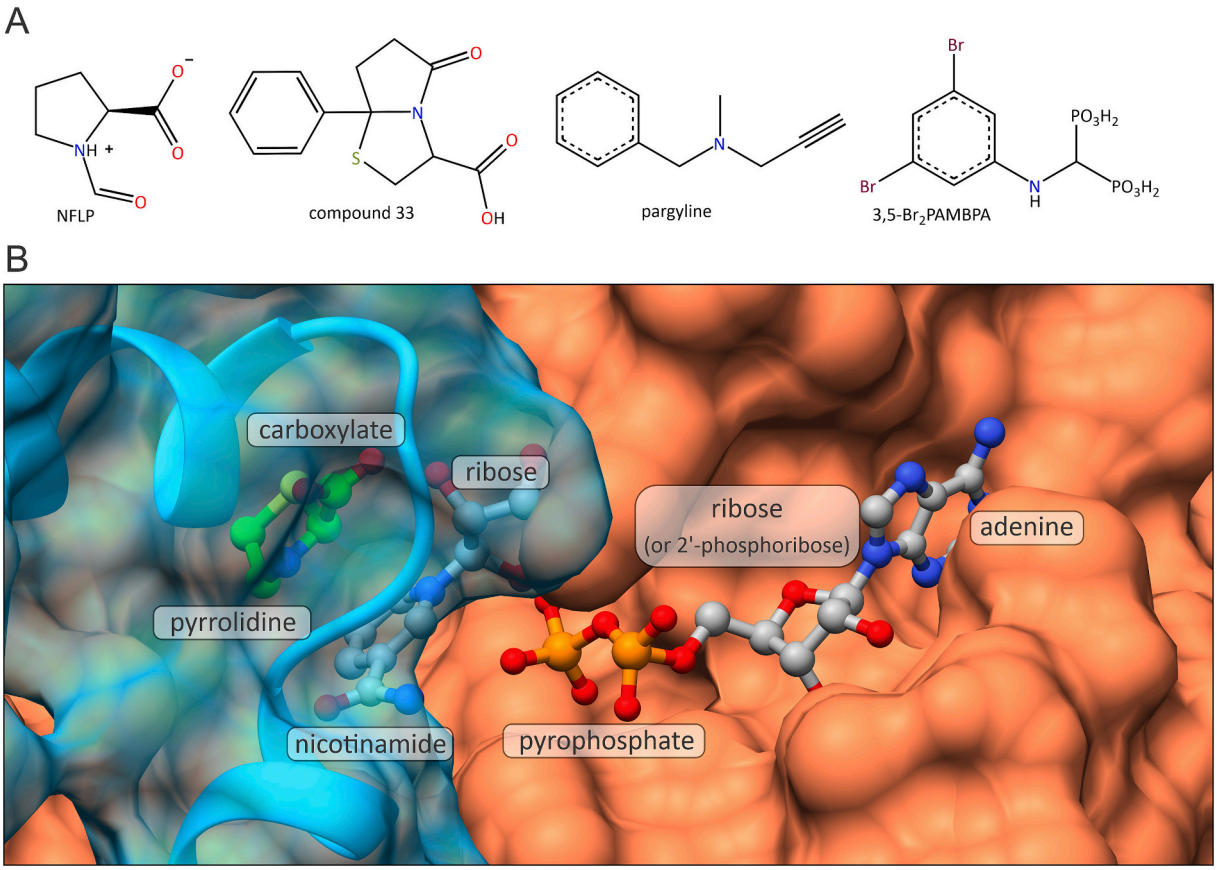


**Fig. 1.** (A) Known inhibitors of PYCR1. Compound 33 was reported by Meeks et al. [32]. (B) Microenvironments (subpockets) within the PYCR1 active site. The surface of one PYCR1 subunit is colored red, while that of the obligate dimer is blue and semitransparent. (For interpretation of the references to colour in this figure legend, the reader is referred to the web version of this article.)

A more chemically diverse approach was undertaken by Milne et al., who employed the LOPAC library consisting of 1280 pharmacologically active, clinically approved compounds. The most promising candidate identified was pargyline, a monoamine oxidase inhibitor, with an $IC_{50}$ of 198 μM (Fig. 1A) [33]. As Sir James Whyte Black said, "The most fruitful basis for the discovery of a new drug is to start with an old drug" [34,35]. This approach offers the advantage of known ADME-Tox properties. However, one must remember that this strategy also entails a narrow activity spectrum. Compounds like pargyline, which have had to demonstrate low off-target effects before their introduction to the market, often have limited affinity for newly proposed targets.

To date, the most potent PYCR1 inhibitor identified is 3,5-dibromophenylamino-methylenebisphosphonic acid (3,5-$Br_2$PAMBPA), which demonstrates an $IC_{50}$ of 0.5 μM (Fig. 1A) [36]. Structure-activity relationships have been established for several other phenyl-substituted aminomethylene bisphosphonates [37]. Despite this promising activity, the lack of structural information regarding their binding sites (an issue shared with pargyline) makes further optimization blindfolded.

Like most P5C reductases, human PYCR1 adopts a homodecameric architecture composed of five dimers arranged in a circular configuration. This quaternary structure positions the ten catalytic sites along a peripheral groove. Each active site is formed at the interface of two subunits within a dimer, making the dimers obligatory for enzymatic function. The NAD(*P*)H coenzyme binds within the N-terminal domain, which features a canonical Rossmann fold, while the substrate, P5C, occupies a pocket formed by a loop connecting α-helices in the C-terminal domain (Fig. 1B) [38]. This spatial arrangement brings P5C into close proximity with the nicotinamide ring of NAD(*P*)H, enabling the hydride transfer required for P5C reduction to proline. The architecture of the PYCR1 active site, at the same time, potentially offers opportunities for targeting several local microenvironments that normally bind pyrrolidine, carboxylate, nicotinamide, ribose, pyrophosphate, another ribose, and adenine (Fig. 1B).

In this study, we present the first crystallographic fragment screening (XFS) campaign targeting human PYCR1, designed to address the limitations of previous efforts by substantially broadening the explored chemical space. Whereas prior studies focused primarily on substrate mimics [31,32], our approach leverages the F2X-Entry screen, a chemically diverse library of 96 low-molecular-weight fragments that are structurally distinct from canonical substrates. This allowed us to interrogate both the P5C and NADH binding pockets of PYCR1.

Importantly, several compounds induced localized conformational shifts in PYCR1, highlighting the dynamic nature of the active site and reinforcing the utility of XFS for uncovering cryptic binding sites. Together, these findings provide a structurally resolved starting point for fragment expansion *via* growing, linking, or merging strategies [38], and establish a versatile framework for the rational development of potent, dual-site PYCR1 inhibitors. In doing so, our study expands both the structural and chemical landscape of PYCR1-targeted inhibition and directly addresses a key bottleneck in translating the enzyme's emerging cancer relevance into therapeutic strategies.

## 2. Results and discussion

### 2.1. Crystallographic fragment screening against a broad chemical space library revealed new PYCR1 binders

A prerequisite for a successful XFS campaign is a reproducible and robust crystallization pipeline capable of generating high-quality crystals, ideally diffracting to a resolution better than 2.2 Å. Equally important is the crystal's stability during soaking with small molecules, which requires tolerance to ~5 % DMSO. In our hands, the most reliable crystallization condition was obtained using the Morpheus screen (Molecular Dimensions) [39]. This condition includes 20 mM tartrate, which we found to bind at the P5C site in preliminary co-crystallization experiments (see below). Importantly, tartrate at concentrations up to 25 mM did not inhibit the NADH-dependent reduction of P5C by PYCR1 (not shown).

Diffraction data were successfully collected for 94 out of the 96 ligands used for soaking (Supplementary Table S1), which are referred to with their respective positions on the 96-well library plate. ADME properties related to solubility for each ligand are listed in Supplementary Table S2. Importantly, physicochemical properties (e.g., solubility) were considered during the library design [40]. Crystals treated with compounds C7 and D8 partially dissolved, resulting in a loss of diffraction quality. The average resolution of the datasets was 1.83 Å, enabling confident identification of several bound ligands (Fig. 2), including detection of water-mediated hydrogen bonds.

The ligands were identified in a two-step procedure. The first two (D11 and H9) were identified by manual inspection based on strong positive peaks in $F_o - F_c$ difference electron density maps. The structures with those ligands were refined using standard, maximum likelihood protocols in *Phenix.refine* and deposited in the Protein Data Bank (PDB) [41]. We note the existence of residual (positive and negative) $F_o - F_c$ densities near the ligands; they could not be interpreted as alternative conformations or partially bound other ligands. Noise in this region most likely reflects the pronounced conformational dynamics of the surrounding protein chain (see below), and heterogeneity within the active site, which may contain a mixture of water, glycol, tartrate, formate, acetate, and oxamate, in addition to the ligand.

In the second step, we implemented the PanDDA software to detect weakly bound molecules in event (*E*) maps [42]. In the latter case, a ligand was considered detected if at least 90 % of its atoms were covered by the *E*-map contoured at the 2σ level. Nonetheless, possibly due to apparent low occupancy, reciprocal-space refinement of those structures resulted in ligands "escaping" the bound sites. Therefore, in addition to manual model editing in Coot, we implemented the real-space refinement protocol in *Phenix.refine* to fit the models in the *E*-maps and ensure proper geometry. The structures were validated with MolProbity [43] and deposited in MX-RDR (https://mxrdr.icm.edu.pl/) together with the *E*-maps and raw diffraction data.

### 2.2. Fragments occupying the P5C/proline site

Tartrate (sequestered from the crystallization solution) occupies the P5C/proline binding site and forms several hydrogen bonds that stabilize its interaction with the protein (Fig. 3A). The electron density maps clearly indicate selective binding of the L-enantiomer. The tartrate hydroxyl groups form direct hydrogen bonds with the side chain of Ser233 and the amide group of Ala237. In addition, one of the tartrate carboxyls participates in hydrogen bonding with the backbone amides of Ser233 and Thr238, as well as the side chain of Thr238. The second carboxyl group forms hydrogen bonds with the side chain of Lys71 and the amide of Ala97. Additionally, three water molecules contribute to the stabilization of the tartrate-protein complex by mediating interactions with Ala97, Ser233, and Ile239.

The first *bona fide* ligand occupying the P5C/proline binding site was compound D11 from the F2X-Entry library. Key residues involved in the PYCR1-D11 interaction include Ala237 and Thr238, both of which form direct hydrogen bonds of 2.9–3.0 Å with the ligand's carboxylate group (Fig. 3B). Additional stabilization is conferred by a network of three water molecules that mediate hydrogen bonding (ranging from 2.7 to 3.2 Å). These H-bond bridges form between the D11's nitrogen atom, water, and Ala97, as well as between D11's carboxylate group, water, Ser233, and Ile239 (Fig. 3B). These interactions are further reinforced by the macrodipole of the α-helix (Ala237 to Gly248) initiated at Ala237, a feature commonly observed in PYCR1 complexes with proline analogs [32]. Additionally, the third water-mediated hydrogen bond links the ligand with the hydroxyl group of Ser233 (not shown in the figure). Notably, ligand binding is further supported by an S-π interaction between the thiazole moiety of D11 and the sulfur atom of Met121 (~3.4-Å distance), as well as hydrophobic interactions between the

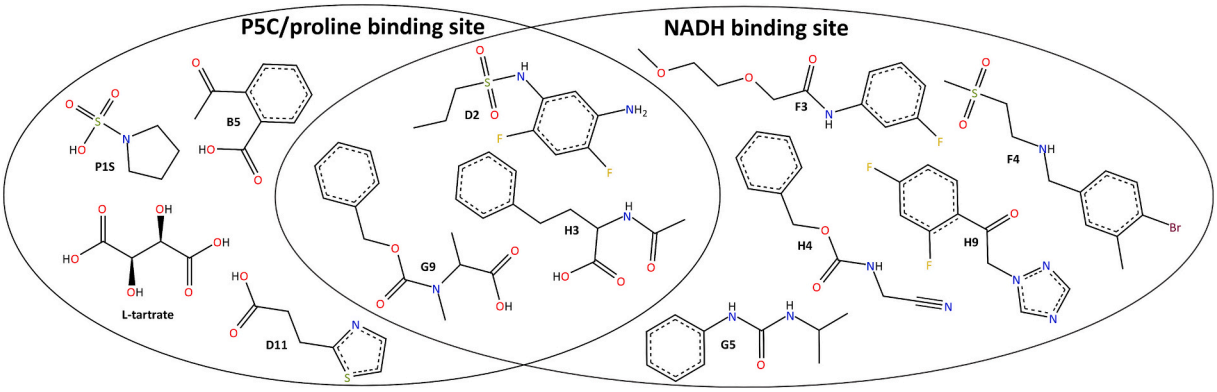


**Fig. 2.** PYCR1 binders identified in this work. The ligands are named according to their position in the plate of the F2X-Entry library. The ligands are divided into three groups: the occupiers of P5C, NADH, or both of these binding sites. Pyrrolidine-1-sulfonate (P1S) and L-tartrate are also included.

thiazole ring and Leu11.

Compared to P5C or proline, the five-membered thiazole ring of D11 is separated from the carboxylate group by two additional carbon-carbon bonds. This extended linker results in a spatial displacement, placing the thiazole moiety in partial overlap with the NADH binding site. Structural analysis suggests a potential steric clash, as indicated by a 1.2 Å distance between the thiazole ring and the C5 atom of the nicotinamide ring (Fig. 3B, inset). To evaluate the inhibitory potential of D11, we determined its half-maximal inhibitory concentration ($IC_{50}$) under saturating concentrations of both P5C and NADH (Fig. 4). The resulting $IC_{50}$ value of 2.74 ± 0.14 mM classifies D11 as a weak inhibitor.

Among the compounds identified with PanDDA, B5 emerged as the only ligand exclusively occupying the substrate-binding site (Fig. 3C). Similar to other P5C analogs, B5 engages in hydrogen bonding with the hydroxyl group of Thr238 and the backbone amide of Ala237. Additionally, the ligand's carboxylate group participates in a water-mediated hydrogen bond network involving residues Ser233 and Ile239. Beyond polar interactions, the binding of B5 is further stabilized by van der Waals interactions with Ala97 and Met121, as well as through the S-π interaction between its aromatic ring and the sulfur atom of Met121.

### 2.3. Fragments overlapping with NADH

Kinetic and structural data indicate that substrate binding in PYCR enzymes follows an ordered sequential mechanism in which L-P5C binds to the enzyme before NAD(*P*)H. A surface rendering of the active center of the enzyme from various organisms shows that, upon binding of the coenzyme, the entrance to the active center cavity is effectively blocked, leaving only a small opening insufficient for P5C entry (Fig. 1B). Consistently, the inhibition of plant P5C reductase by phenyl-substituted aminomethylenebisphosphonates was found incompetitive with respect to P5C [44]. Product inhibition studies led to the same conclusion for human PYCR2 [45]. Therefore, binders to the NADH pocket could also prevent P5C binding. The *Fo − Fc* difference electron density maps revealed a clear and continuous signal for compound H9, which was modeled and refined at full occupancy alongside tartrate, bound as described above (Fig. 5A). H9 binds exclusively to the coenzyme binding site, overlapping with both nicotinamide and ribose moieties of NADH. The ligand establishes a single hydrogen bond, mediated by a water molecule, with the backbone carbonyl of Val231. In addition, the *para*-fluorine forms an orthogonal C—F···C═O interaction with the backbone of Asn123 at a distance of 3.0 Å. The *ortho*-fluorine interacts with Cys95, Cys120, and Thr122 *via* a water molecule with H-bonds ranging ~3.0 Å. Notably, comparison with the D11-bound structure reveals that H9 induces a conformational rearrangement discussed in detail in a separate section.

To evaluate its functional relevance, we assessed whether H9 inhibits PYCR1 activity under near-saturating substrate conditions (2.5 mM P5C and 500 μM NADH). No inhibitory effect was observed, even when co-incubated with equimolar concentrations of tartrate (data not shown). This result is consistent with the typical properties of fragment-sized ligands identified by crystallographic screening, which often display weak or no activity prior to optimization. Moreover, H9 and any ligand binding at the coenzyme site must compete with NADH, for which PYCR1 has a significantly higher affinity ($K_M = 88$ μM) compared to that of P5C ($K_M = 714$ μM) [36]. In other words, a ligand occupying the NADH site would need to exhibit inhibitory properties at concentrations comparable to the $K_M$ of NADH to be detectable. On this basis, we decided not to test the inhibition brought about by other ligands that also occupy the NADH binding site.

The remaining ligands binding at the NADH pocket were identified through PanDDA-based analysis of *E*-maps [34]. Among these, compounds F3, F4, G5, and H4 localize exclusively to the cofactor-binding site (Fig. 5B–E).

Ligand F3 directly overlaps with the ribose moiety of NADH (Fig. 5B). It forms a direct hydrogen bond as a proton acceptor from the side chain of Lys71. Additional water-mediated hydrogen bonds involve the ligand's amine group, with a surrounding water molecule facilitating the interactions. These polar contacts are further stabilized by hydrophobic interactions with residues Leu11, Ala14, and Ala96. A notable orthogonal C—F···C═O interaction is observed between the ligand's fluorine substituent and the carbonyl group of Gln10 (3.1 Å), contributing to binding specificity.

Compound F4 occupies both the ribose and nicotinamide subpockets within the NADH-binding site (Fig. 5C). The PYCR1-F4 complex is stabilized primarily through a network of water-mediated hydrogen bonds involving the ligand's secondary amine and the backbone atoms of Cys95, Cys120, and Thr122. In this structure, tartrate is also present, and one of its hydroxyl groups forms a hydrogen bond with the F4 sulfonyl group. In addition, the *para*-bromine substituent of F4 engages in halogen bonding with the backbone carbonyl of Gln10 (3.5 Å). Hydrophobic contacts further support complex stability, particularly with residues Leu11, Ala96, Thr122, and Thr124.

Ligand G5 occupies a region adjacent to the ribose-binding subpocket (Fig. 5D). Although it forms only a single, water-mediated hydrogen bond with the carbonyl group of Cys95, it is retained in the binding pocket through van der Waals interactions with a hydrophobic patch composed of Leu11, Ala14, Ala96, and Thr122.

The phenyl moiety of compound H4 also occupies a peripheral region of the NADH site near the nicotinamide subpocket and forms extensive hydrophobic interactions with nonpolar side chains of Leu11, Ala14, Thr122, Thr124, and Val126 (Fig. 5E). However, the nitrile group extends toward the P5C/proline site, forming a direct hydrogen bond with the hydroxyl group of Ser233.

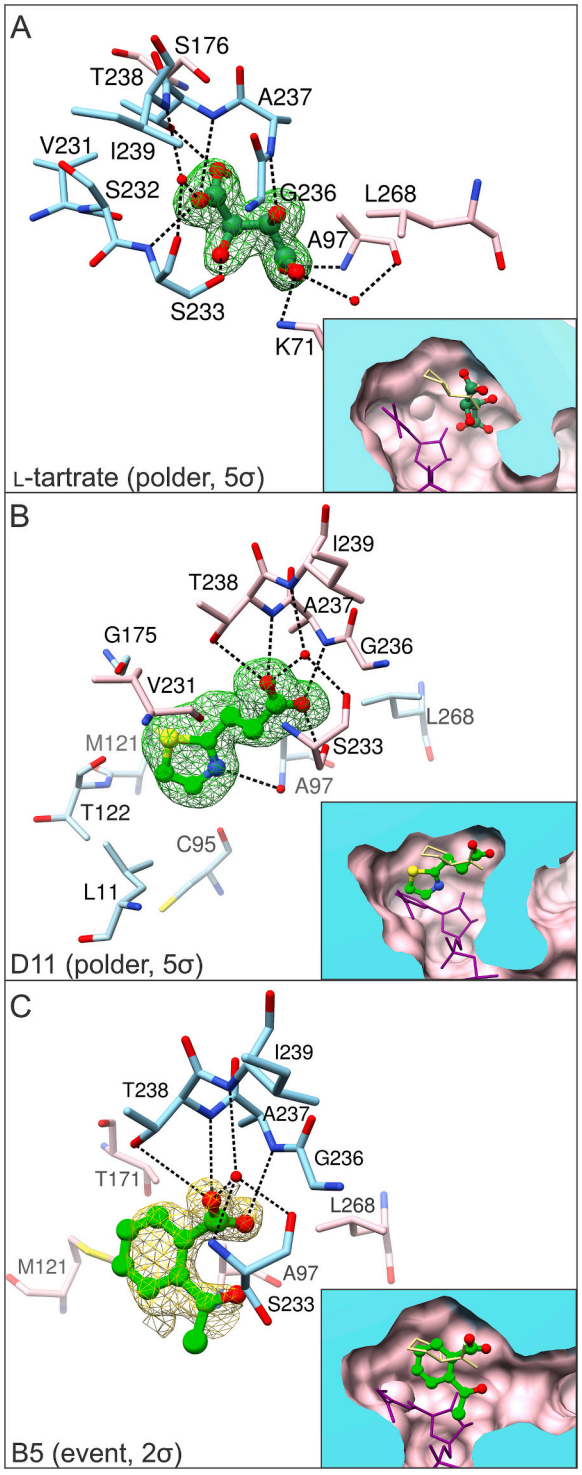


**Fig. 3.** Ligands that bind at the substrate binding site and their interactions. (A) L-tartrate; the green mesh represents the polder electron density map ($F_o - F_c$). (B) Ligand D11. (C) Ligand B5 with *E*-map shown as a yellow mesh. Map contours are marked on panels for each compound. Depicted amino acid residues are located within 4.0 Å from ligands. Dashed lines represent hydrogen bonds. The inset shows the superposition of the ligand with the P5C analog (yellow) and NADH (dark purple) in a stick representation, and PYCR1 shown as a surface clipped for clarity. (For interpretation of the references to colour in this figure legend, the reader is referred to the web version of this article.)

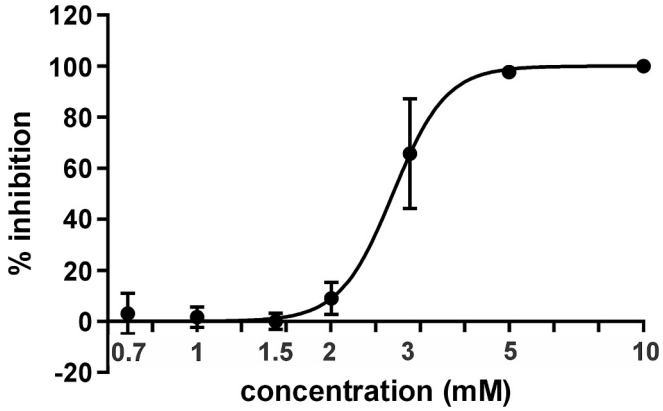


**Fig. 4.** The $IC_{50}$ curve for compound D11. The $IC_{50}$ value was determined based on the absorbance at 340 nm. The measurements were performed for 7 concentrations of D11: 700 μM, 1 mM, 1.5 mM, 2 mM, 3 mM, 5 mM, and 10 mM under saturating concentrations of both P5C and NADH. PYCR1 was used at a final concentration of 0.24 μg/mL.

### *2.4. Dual-site binders overlapping with both P5C and NADH: ligands D2, G9, and H3*

Compounds D2, G9, and H3 occupy both the substrate (P5C) and cofactor (NADH) pockets of PYCR1. More precisely, the non-aromatic regions of these ligands overlap with the pyrroline ring of P5C, while their aromatic moieties extend into the NADH binding site.

The binding of ligand D2 is anchored through a combination of direct and water-mediated hydrogen bonds (Fig. 5F). The amine substituent of the ligand forms direct hydrogen bonds with the carbonyl group of Val70, while the sulfonamide group, through its O atoms, interacts with the backbone amides of Ala237 and Thr238. Additionally, a hydrogen bond is formed between the ligand amide and the side chain hydroxyl of Ser233. Water-mediated hydrogen bonding further stabilizes the complex, involving interactions between the ligand's *meta*-amine group and the backbone carbonyl of Ala97, as well as between the sulfonamide group and the backbone carbonyl of Ser233. Notably, an orthogonal C—F···C═O interaction is observed between the *para*-fluorine atom of the ligand and the carbonyl groups of Ala69 and Val70, both at distances of 3.2 Å. Additional stabilization arises from hydrophobic contacts with Ala97 and Thr171.

Ligand G9 engages in a single hydrogen bond with the side chain of Ser233 (Fig. 5G). Despite the limited polar interactions, the ligand is retained within the active site through hydrophobic interactions with Leu11, Ala97, Thr122, Thr124, and Thr171.

Ligand H3 is anchored within the active site of PYCR1 *via* a hydrogen bond network involving its carboxylate group and the side chain of Thr238, along with the backbone amides of Ala237 and Ser233 (Fig. 5H). Further stabilization is achieved through van der Waals interactions with the nonpolar residues Leu11, Ala97, Thr124, and Thr171.

### *2.5. Sulfur oxyanions as isosteric carboxylate replacements*

Since PYCR1 is predominantly localized within the mitochondria, any effective PYCR1-targeted therapeutic must be capable of traversing not only the cellular membrane but also the mitochondrial double membrane. This poses a considerable challenge, particularly because the P5C/proline binding site is optimized for interactions with a carboxylate group, whose permeability *via* passive diffusion is limited.

Previous studies have demonstrated that the carboxylate group can be substituted with a sulfonate group in PYCR1-targeted proline analogs [46]. However, comprehensive analyses of carboxylate bioisosteres have revealed that sulfonates exhibit lower membrane permeability

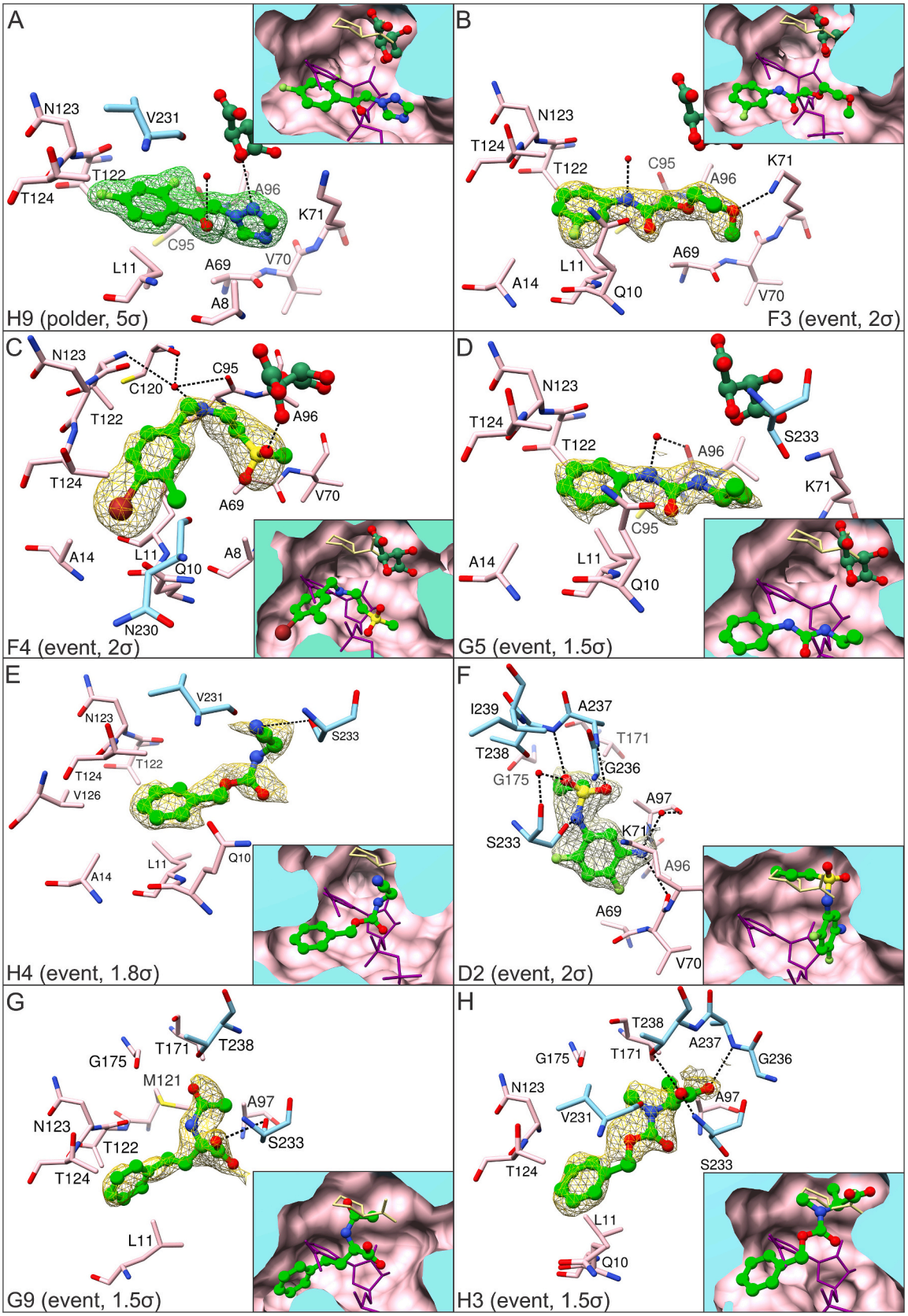


**Fig. 5.** Ligands that bind at the cofactor binding site and their interactions; dual-site binders are also included. The polder electron density maps are shown as a green mesh. Event-maps are shown as a yellow mesh. Map contours and types are marked on each panel. Depicted amino acid residues are located within a 4.0-Å distance from ligands. Dashed lines represent hydrogen bonds. Each inset shows the superposition of the ligand with the P5C analog (yellow) and NADH (dark purple). (For interpretation of the references to colour in this figure legend, the reader is referred to the web version of this article.)

compared with carboxylates [47]. In this context, the identification of a sulfonamide group in ligand D2, occupying the carboxylate-binding site (Fig. 5F), appears especially promising. Sulfonamides generally offer improved ADME properties, including enhanced membrane permeability, when compared with both carboxylates and sulfonates.

We decided to further explore this path and investigate a P5C/proline analog bearing a sulfamate moiety, pyrrolidine-1-sulfonate (P1S). Notably, the binding of sulfamates to PYCR1 has not been studied previously. As P1S is not available commercially, we used pyrrolidine-1-sulfonyl chloride, which undergoes spontaneous hydrolysis in aqueous solution to yield P1S. The resulting crystal structure confirmed that P1S binds in a manner similar to proline (Fig. 6A). The major role in stabilizing the PYCR1-P1S complex is played by hydrogen bonds involving the sulfamate oxygens. One of them forms hydrogen bonds with the backbone amide group and the hydroxyl moiety of Ser233. The second oxygen of the sulfamate forms a hydrogen bond with the backbone amide of Ala237. The third oxygen is H-bonded to Thr238, involving both the main-chain and side-chain of this residue. Additionally, it participates in water-mediated hydrogen bonding that connects the ligand with the backbone carbonyl of Ser233 and amide of Ile239.

When measured at saturating substrate concentrations, P1S exhibited an $IC_{50}$ of 1.88 ± 0.159 mM, indicating weak inhibitory activity (Fig. 6B). This value is comparable to that of proline, which has a reported Ki of 1.7 mM [31]. Furthermore, the presence of an additional hydroxyl group in the ligand could potentially enhance binding, as observed for 1-hydroxyethane-1-sulfonate (PDB ID: 8TDB), referred to as compound 43 in the original work [46] (Fig. 6C). In this case, the hydroxyl group donates a hydrogen bond to the Val231 carbonyl and accepts one from the Thr238 side chain. These interactions likely explain the higher apparent efficacy of compound 43 (Ki = 100 μM), although the assay conditions differed. However, the sulfamate group presents an attractive handle for further ligand optimization to improve potency. Notably, P1S forms a hydrogen bond with the hydroxyl group of Ser233, whose critical role in ligand recognition was previously demonstrated [31]. Therefore, sulfonate (as in compound 43), sulfonamide (compound D2), and sulfamate (P1S) appear to be viable isosteric replacements for carboxylate in the PYCR1 active site.

### 2.6. PYCR1 flexibility and adaptability of the active site pocket

During the PYCR1-H9 structure refinement, it became apparent that the conformation of the protein chain differed significantly from that in other complexes, such as PYCR1-D11 (Fig. 7A). In fact, the PYCR1 complexes reported in this work can be divided into two classes: one representing states similar to that observed in PYCR1-TLA or D11 complexes and the other resembling PYCR1-H9 (Fig. 7B). The observed shifts of more than 5 Å indicate an induced-fit binding mode. Notably, the crystal lattice in all our structures is isomorphous, and therefore, the protein conformations can be attributed purely to ligand presence rather than crystal packing. In terms of protein chain conformation, previously published PYCR1 structures differ significantly from PYCR1-H9, and are more similar to the PYCR1-D11 complex (Fig. 7C). Certain flexibility near the PYCR1 active site had already been observed by Christensen et al. [31]. The authors noted that in the PYCR1-NFLP complex (PDB ID: 6xp0), the α-helix spanning Pro224-Val231 (denoted αK) is shifted by ~1 Å toward its N-terminus. That conformational change was required to accommodate the formyl group of NFLP and allow it to form additional H-bonds with Ser233.

With that in mind, the structural rearrangements observed in the PYCR1-H9 complex are truly spectacular. The shifts involve three regions near the ligand-binding site (Fig. 7A). The region Ile6-Ala12 is significantly closer to the ligand, with the largest movement observed for Ala8 (5.0 Å shift of Cα) compared with the PYCR1-D11 structure. The fragment Ser33-Asp38 shifts along with the former, involving a 5.4-Å change in the Met37 Cα position. Regarding the Ile6-Ala12 and Ser33-Asp38 regions, the structures reported in this work can be divided into

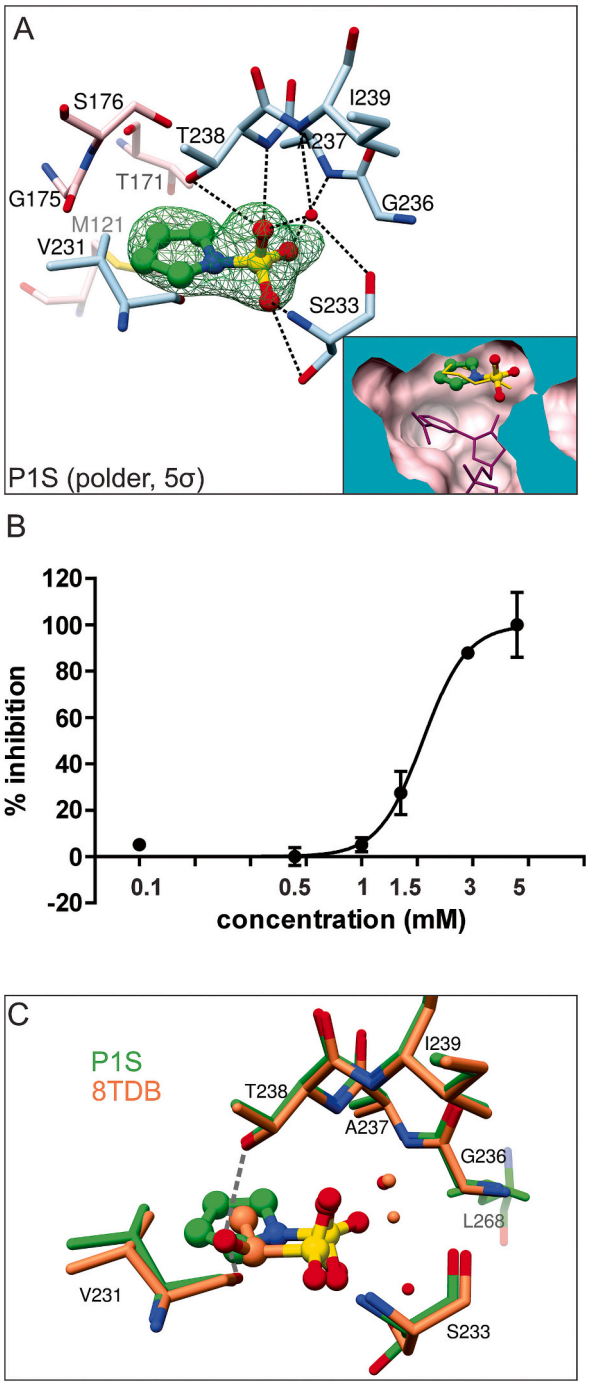


**Fig. 6.** Interactions with pyrrolidine-1-sulfonate (P1S). (A) P1S with the polder electron density maps ($F_o - F_c$) is shown as a green mesh. Dashed lines represent hydrogen bonds. The inset shows the superposition of the ligand with the P5C analog (yellow) and NADH (dark purple). (B) The $IC_{50}$ curve for P1S, measured under saturating substrate concentrations (2.5 mM P5C and 500 μM NADH). (C) Superposition of PYCR1-P1S complex with the structure of PYCR1 complexed with NADH and 1-hydroxyethane-1-sulfonate (PDB ID: 8TDB), referred to as compound 43 in the original work [46]. Grey dashed lines represent the additional hydrogen bonds formed by the hydroxyl of compound 43; the remaining interactions are omitted for clarity. (For interpretation of the references to colour in this figure legend, the reader is referred to the web version of this article.)

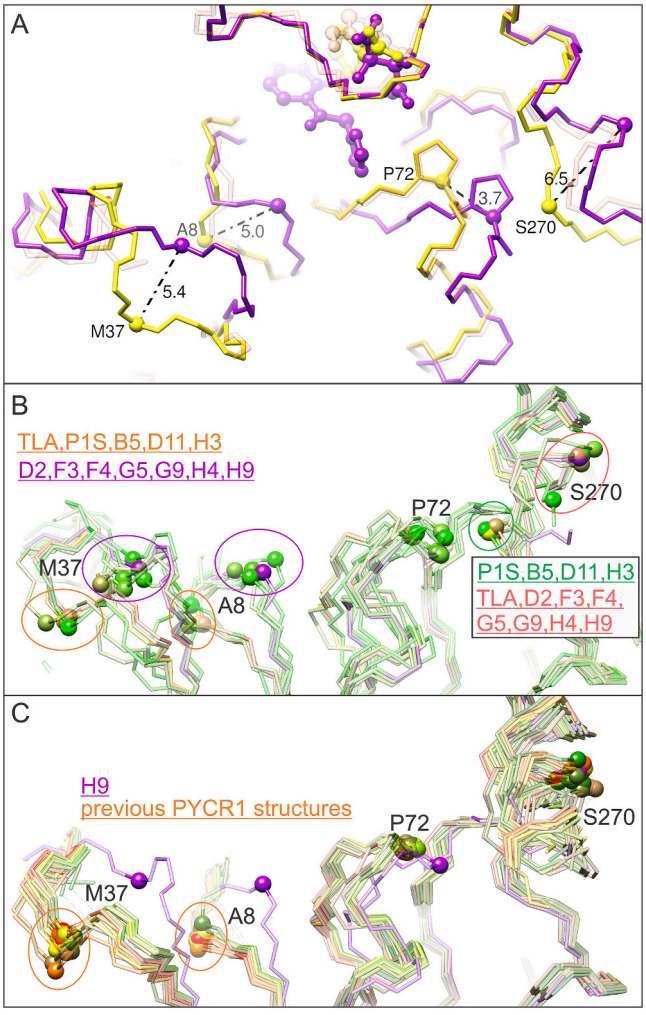


**Fig. 7.** Structural rearrangements upon ligand binding. (A) The PYCR1-D11 (yellow) and H9 (purple) complexes were superposed; the PYCR1-NFLP complex (PDB ID: 6xp0, coral, semi-transparent) is added for comparison as the example for which structural changes were described by Christensen et al. [31]. Cα atoms of residues undergoing the largest shifts (dash-dotted lines; distances in Å) and referenced in the text are shown as balls, and those in the PYCR1-D11 complex are labeled. Ligands are depicted in ball-and-stick representation. Residues are labeled in black. (B) PYCR1 main-chain conformations in all PYCR1 structures reported in this work. Positioning of regions near Ala8, Met37, Pro72, and Ser270 is colour-coded. Note that the conformations of regions near Ala8 and Met37 are not always correlated with those of the region near Ser270. (C) Comparison of the main chain conformation in this work PYCR1-H9 complex with those in all other structures available in the PDB (PDB IDs: 8TCV, 8TCX, 8TCZ, 8TCU, 8TCW, 8TCY, 8TD0, 8TD1, 8TD7, 6XP0, 6XOZ, 6XP1, 6XP2, 6XP3, 8TD2, 8TD3, 8TD4, 8TD5, 8TD6, 8TD8, 8TD9, 8TDB, 8TDC, 8TDD, 8VRE, 8DKG, 5UAX, 5UAT, 5UAU, 5UAV, 5UAW). Chains other than A are omitted for clarity in panels B and C. (For interpretation of the references to colour in this figure legend, the reader is referred to the web version of this article.)

two groups: (i) TLA, P1S, B5, D11, H3, resembling the conformations observed previously; and (ii) D2, F3, F4, G5, G9, H4, H9, whose main-chain arrangement is different (Fig. 7B). Notably, Asp36-Asp38 are absent in the PYCR1-NFLP model because of insufficient electron density. The third fragment whose conformation was altered is Leu68-Ile78. In particular, Pro72 shifted by as much as 3.7 Å (Cα positions in D11 vs. H9). The latter rearrangement appears to be directly induced by the H9 ligand binding, as the protein adjusts to fit the triazole moiety. On the other hand, the protein conformation in the PYCR1-D11 complex differs from that in both the H9 and NFLP complexes within the C-terminal region (residues Gln269-Asp273). Ser270, which undergoes the largest shift of 6.5 Å (Cα atoms), is closer to the active site and to Pro72 in the PYCR1-D11 complex.

The ability of PYCR1 to rearrange and accommodate binders of such diverse chemical structures and sizes is exceptional. We wondered whether these extreme states are the product of a ligand-induced fit mechanism or are already present in the conformational landscape of PYCR1. To shed new light, we performed 1-μs all-atom molecular dynamics (MD) simulations on the PYCR1 structures derived from the D11 and H9 complexes without the ligands (Supplementary Fig. S1). As the indicator, we selected the Pro72(Cα)–Val231(Cα) distance, since Val231 lies along the axis of movement associated with shifts in the position of Pro72(Cα). Of note, this distance measures 14.6 and 18.4 Å in the PYCR1-D11 and H9 crystal structures, respectively. Measurement of the distances across the simulation trajectory for each subunit individually yielded an average of 15.6 ± 0.8 and 16.5 ± 0.8 Å, respectively (Supplementary Table S3). More importantly, the maximal distance of 19.7 Å was actually observed in the MD run starting from the PYCR1-D11 conformation. This suggests that, while an initial bias exists due to the wider opening of the H9 complex, the intrinsic conformational flexibility of PYCR1 can produce states corresponding to those observed in both the D11 and H9 complexes.

## 3. Conclusions and outlook

Previous studies, especially those reporting a number of PYCR1–inhibitor complexes [31,32,46], have firmly established the chemical tractability of PYCR1. They also highlighted its intrinsic flexibility, providing the first evidence of induced-fit behavior. Building on this foundation, our crystallographic fragment screening (XFS) campaign offers the first structure-based exploration of PYCR1's ligand-binding landscape using a chemically diverse, unbiased library.

Our crystallization system contained tartrate, which was bound in the "empty" structures and in complexes with H9, F3, F4, and G5. Complexes with P1S, D11, D2, B5, H3, G9, and H4 did not contain it, i.e., these ligands displaced tartrate, indicating also that a cleared active site is not a prerequisite for XFS. In total, twelve previously uncharacterized ligands were identified within the P5C and NADH binding pockets, including dual-site binders that bridge both regions. High-resolution crystal structures revealed a network of interactions spanning distinct microenvironments within the active site. In several cases, ligand binding induced prominent conformational rearrangements, which, in the extreme case of the PYCR1-H9 complex, included main-chain shifts of 4–6 Å. The observed conformations of the PYCR1 main chain appear directly correlated with ligand chemical structure and binding position, allowing identification of certain compound classes. Importantly, extreme states such as that observed in the PYCR1-H9 complex have not been observed in the many known PYCR1 structures. Molecular dynamics simulations demonstrated that these conformational states fall within the intrinsic flexibility of PYCR1, confirming the enzyme's structural adaptability and capacity to recognize a broad range of chemical scaffolds.

A residue-level analysis of fragment binding revealed distinct interaction hotspots that correspond to specific moieties of the substrate and cofactor binding sites in PYCR1. In the carboxylate-binding region, Ser233, Ile239, and Ala97 form an extensive polar network—either directly or through structured water molecules—that stabilizes the binding of fragments such as D11 and B5, which feature carboxylate groups, or fragments D2 and P1S, which carry sulfonamide and sulfamate moieties. The latter two are particularly notable for their improved ADME properties, especially enhanced membrane permeability compared with carboxylates. The binding interactions are further reinforced by the dipole of the helix beginning at Ala237, a structural hallmark of the P5C/proline-binding site. The pyrrolidine-binding subpocket can accommodate an aromatic ring when appropriately substituted, as in B5, where a carboxylated phenyl overlaps this position.

In two cases, aliphatic and saturated chains occupy the pyrroline site: an ethyl linker in D11, or a propyl group in D2. Interestingly, the thiazole of D11 is positioned between the pyrroline and nicotinamide subpockets. The nicotinamide-binding site is defined by key interactions with Val231, Asn123, and Thr122. Compound H9 features a fluorinated phenyl ring that engages in an orthogonal C—F···C═O interaction with the backbone of Asn123. Notably, several binders containing an aromatic moiety (H9, F3, F4, G5, H4, G9, H3) access a cryptic subpocket shaped by Leu11, Thr122, and Thr124, which extends deeper than typically observed for nicotinamide binding (Fig. 5). Additional stabilizing interactions include halogen bonding between F4 and Gln10, as well as π-sulfur interactions, exemplified by D11···Met121. In the ribose-binding subpocket, ligands F3 and F4 engage Cys120, Thr122, and Lys71 through hydrogen bonds, either directly or *via* bridging water molecules. This region is further supported by hydrophobic contacts involving Ala14, Ala96, and Val70. Finally, a continuous hydrophobic patch spanning the substrate and cofactor sites contributes van der Waals interactions that stabilize multiple ligands, including dual-site binders such as G9 and H3.

Our findings collectively show that PYCR1 is not only chemically tractable but also highly adaptable and capable of interacting with a broad repertoire of chemical moieties. Future efforts should focus on fragment linking and extension into underexplored subpockets, particularly near the NADH adenosine and phosphate regions. Importantly, the observed conformational plasticity underscores the need for design strategies that account for dynamic ensemble states rather than static models. These structural insights provide a compelling starting point for the rational development of PYCR1 inhibitors and effectors, advancing its emerging potential as an intervention point in cancer treatment.

## 4. Materials and methods

### 4.1. Cloning

The construct for PYCR1 production was designed based on the work by Christensen et al. [38]. The N-terminal methionine of the genuine PYCR1 sequence was preceded by MHHHHHHSSGVDLGTENLYFQS. Moreover, we found that C-terminal truncation following Asp273 greatly increases repeatability; hence, our construct included residues 1–273 of the 319-residue full-length variant (Uniprot ID: P32322). To obtain the designed construct, total RNA was isolated from human MCF-7 cells using the Universal RNA Purification Kit (EurX). The isolated RNA was subsequently reverse transcribed into cDNA using Maxima H-reverse transcriptase. The desired DNA fragment was amplified by polymerase chain reaction (PCR) with the primers: forward TACTTCCAATCCAATGCCATGAGCGTGGGCTTCATCGGC and reverse TTATC CACTTCCAATGTTAGTCAGCCATGGACTGCAGCTC. Amplified DNA fragments were cloned into the pMCSG53 vector using a ligase-independent procedure [48] and subsequently transformed into *E. coli* BL21 Gold (Agilent) competent cells. The following primers were used to modify the N-terminal region: ACCTGGGCACCGAGAACCTCTATTTCCAATCGATGAGCGTGGGCTTCATCGGC (forward) and GAGGTTCTCGGTGCCCAGGTCCACGCCGCTGCTGTGATGATGATGATGGTGCATATGTATATCTCCTTC (reverse) according to the Polymerase Incomplete Primer Extension protocol [49]. The coding sequence was verified by DNA sequencing.

### 4.2. Protein production

PYCR1 production in *E. coli* was performed in 1 L of liquid LB medium supplemented with 150 μg/mL ampicillin. The bacterial culture was shaken at 37 °C until the $OD_{600}$ reached 1.0. The temperature was then lowered to 4 °C, and shaking was continued for 1 h. Overexpression was induced using 0.5 mM isopropyl-D-thiogalactopyranoside (IPTG) and continued overnight at 18 °C. The cells were harvested by centrifugation at 6000 ×*g* for 15 min, and resuspended in binding buffer (50 mM HEPES NaOH, pH 8.0; 300 mM NaCl; 50 mM imidazole; 5 % glycerol). The suspension was frozen and stored at −80 °C.

### 4.3. Protein purification

Cells were lysed by sonication in an ice bath with a total probe working time of 5 min (4/26 s on/off cycles). Cell debris was removed by centrifugation (27000 ×*g*, 30 min, 4 °C). The supernatant was applied to a column filled with HP Ni-NTA resin (GE Healthcare). The resin-bound protein was washed with 250 mL of binding buffer and eluted with 12 mL of elution buffer (50 mM HEPES NaOH, pH 8.0; 300 mM NaCl; 300 mM imidazole; 5 % glycerol). The $His_6$-tag was not cleaved. The collected protein was concentrated to 2 mL using Amicon Ultra 50 mL centrifugal filters, and then injected into a size-exclusion column (HiLoad Superdex 200 16 × 60) connected to the AKTA FPLC system (GE Healthcare). Chromatography was performed using size-exclusion buffer (50 mM HEPES NaOH, pH 8; 300 mM NaCl; 5 % glycerol). The fractions were analyzed by SDS-PAGE. Fractions corresponding to the PYCR1 decamer were combined and concentrated to ~10 mg/mL.

### 4.4. Protein crystallization

PYCR1 was crystallized at 19 °C by vapor diffusion using the sitting-drop method in Nextal plates (Qiagen). Initial screening was performed with JCSG+, BCS, and Morpheus screens (Molecular Dimensions). Optimal crystals for soaking were obtained from a solution consisting of the Morpheus 2–34 condition [39] (Molecular Dimensions), containing 0.02 M sodium formate, 0.02 M ammonium acetate, 0.02 M sodium citrate tribasic, 0.02 M potassium sodium tartrate, 0.02 M sodium oxamate, 0.1 M Tris (base), BICINE pH 8.5, 20 % ethylene glycol, 10 % PEG 8000, and supplemented with 10 % ethylene glycol for cryoprotection. The protein was mixed with reservoir solution in a *v*/v ratio of 1:1 (2 μL:2 μL) and crystallization seeds.

### 4.5. Crystallographic fragment screening

For crystallographic fragment screening, the F2X-Entry library [40] consisting of 96 chemical fragments was used. The fragments were dissolved in a soaking solution composed of the crystallization solution with an additional 10 % ethylene glycol and 5 % DMSO. The final concentrations of the fragments in the soaking solutions were 33 mM. The PYCR1 crystals were transferred to a solution containing fragments and incubated for 3 min before flash-cooling in liquid nitrogen.

### 4.6. X-ray structure determination and refinement

Diffraction data were collected at the BioMAX beamline of MAX IV [50] and the P13 beamline of PETRA III (EMBL, Hamburg, Germany) [51]. Diffraction images were processed in *XDS* [52]. Data collection and processing statistics are summarized in Table 1. Structures were solved by refinement against the isomorphous structure (PDB ID: 6xp1, [31]) using *Dimple* [53] within the *CCP4* suite [54]. Identification of ligands in *E*-maps was performed with *PanDDA* [42], also implemented in CCP4. Manual corrections were performed using *Coot* [55]. The models were refined in several cycles in *Phenix.refine* [56]. Structures were validated with *MolProbity* [43].

### 4.7. Synthesis of DL-P5C

DL-P5C was synthesized as described previously [57]. Briefly, 2 mmol of hydroxylysine was dissolved in 28 mL of water in a brown glass bottle and cooled to 4 °C. A 50 mM solution of sodium metaperiodate was adjusted to pH 7.0 using 1 M NaOH and also cooled to 4 °C. Then, 44 mL of the neutralized periodate solution was rapidly added to the hydroxylysine solution under stirring. After 8 min, the remaining periodate was quenched with 0.7 mL of 1 M glycerol. Two minutes later, the

**Table 1**
X-ray data collection and refinement statistics.

| | PYCR1-TLA | PYCR1-D11 | PYCR1-H9 | PYCR1-P1S |
|---|---|---|---|---|
| **Data collection** | | | | |
| Beamline | | BioMAX at MAX IV | | P13 at PETRA III, EMBL |
| Wavelength (Å) | | 0.976 | | 1.0597 |
| Temperature (K) | | 100 | | |
| Space group | $P2_12_12$ | $P2_12_12$ | $P2_12_12$ | $P2_12_12$ |
| Unit cell parameter *a*, *b*, *c* (Å) | 164.20, 88.11, 116.25 | 163.67, 88.04, 116.73 | 163.78, 88.00, 116.81 | 164.55 88.04 116.66 |
| Resolution range (Å) | 37.21–1.65 (1.75–1.65)[a] | 37.11-1.65 (1.75–1.65)[a] | 38.64-1.57 (1.67–1.57)[a] | 46.55-1.70 (1.80-1.70)[a] |
| No. of unique reflections | 201,497 (32213)[a] | 202,193 (32339)[a] | 234,708 (37624)[a] | 185,960 (29800)[a] |
| Completeness (%) | 99.9 (99.7)[a] | 100.0 (99.8)[a] | 100.0 (99.9)[a] | 99.7 (99.7)[a] |
| Redundancy | 13.6 (13.8)[a] | 13.7 (13.76)[a] | 13.6 (13.39)[a] | 13.8 (13.3)[a] |
| I/σ (I) | 22.86 (1.45)[a] | 19.84 (1.46)[a] | 20.46 (1.41)[a] | 18.19 (1.47)[a] |
| $R_{meas}$ (%) | 6.1 (210)[a] | 7.7 (205.4)[a] | 6.3 (211.1)[a] | 12 (282.1)[a] |
| $CC_{1/2}$ (%) | 100.0 (72.8)[a] | 100.0 (72.2)[a] | 100.0 (76.0)[a] | 100.0 (45.6)[a] |
| **Refinement** | | | | |
| No. of $R_{free}$ reflections | 1999 | 2000 | 1998 | 1857 |
| $R_{work}/R_{free}$ | 0.182/0.204 | 0.174/0.193 | 0.185/0.205 | 0.191/0.215 |
| No. of non-H atoms | | | | |
| Protein | 10,195 | 10,199 | 10,150 | 10,262 |
| Ligand | 46 | 222 | 154 | 85 |
| Water | 674 | 724 | 810 | 808 |
| R.m.s. deviations Bonds (Å)/ angles (°) | 0.004/0.67 | 0.01/1.01 | 0.006/0.822 | 0.006/0.822 |
| Ramachandran plot Favored/allowed/outliers (%) | 98.60/1.40/0.00 | 98.75/1.25/0.00 | 98.60/1.40/0.00 | 97.87/2.13/0.00 |
| Average B-factor protein/water/ligands ($Å^2$) | 51.83/52.57/54.75 | 42.65/46.43/53.52 | 44.35/47.89/50.67 | 43.84/42.04/43.32 |
| PDB ID | 9s01 | 9s02 | 9s04 | 9rzz |

[a] Values in parentheses are for the last resolution shell.

reaction mixture was acidified with 0.6 mL of 6 M HCl. The mixture was removed from the ice bath and loaded onto a Dowex 50 column. The product was eluted with 1 M HCl and stored at 4 °C in solution. Product identity was confirmed by mass spectrometry.

### 4.8. $IC_{50}$ determination

$IC_{50}$ values at saturating substrate concentrations were measured for compounds identified through difference maps: D11, H9, P1S, and tartrate. The physiological P5C reduction reaction with NADH was monitored by measuring the decrease in absorbance at 340 nm.

Compound D11 and L-tartrate were tested at eight concentrations (10 mM, 5 mM, 3 mM, 2 mM, 1.5 mM, 1 mM, 700 μM, 400 μM). For compound H9, the range was extended to 15, 20, and 25 mM. Compound P1S was tested at six concentrations (5 mM, 3 mM, 1.5 mM, 1 mM, 500 μM, and 100 μM). A 5 % DMSO solution served as a negative control. All D11, H9, and P1S stock solutions were prepared in DMSO, while tartrate was dissolved in Milli-Q water. Final assay concentrations were: 17.6 nM PYCR1, 0.5 mM NADH, and 2.5 mM DL-P5C. PYCR1 was diluted in assay buffer (25 mM Tris, pH 8.0, 100 mM NaCl, 1 mM TCEP), NADH was dissolved in Milli-Q water, and DL-P5C was adjusted to pH 7.0 using Tris base before dilution in assay buffer. Inhibitor solutions (5 μL for ligands revealed during XFS and 0.75 μL for P1S) were dispensed into wells of a microtiter plate, followed by the addition of 33 μL (50 μL in the assay with P1S) of the PYCR1 solution. After a 15-min incubation, 33 μL of NADH and 33 μL of P5C were added (50 μL NADH and 50 μL P5C in the assay with P1S); the addition of P5C initiated the reaction. The plate was immediately placed in a HIDEX Sense Microplate Reader, and absorbance at 340 nm was recorded every 60 s for at least 15 min. Each $IC_{50}$ measurement was performed in triplicate. Dose–response curves were plotted, and $IC_{50}$ values were calculated in *GraphPad* 6 (Prism) software. The errors were calculated as half of the difference between 95 % confidence interval values.

### 4.9. Molecular dynamics simulations

Models for MD simulations were created from the refined structures of PYCR1-D11 and PYCR1-H9 complexes, each reconstituted into physiologically relevant decamers. Such models were imported into *Maestro 14* within Schrödinger Suite, release 2025-1 (Schrödinger, LLC, New York, NY, 2025) and processed with the protein preparation tool, including the addition of hydrogen atoms, optimization of their geometry, and energy minimization. Except for water molecules, all ligands were removed. In cases of double conformations, only those with the highest occupancies were kept.

The MD simulations were performed in *Desmond 8.1.129* [58], within *Maestro 14* (Schrödinger, LLC, New York, NY, 2025). Each system was configured with the most recent OPLS5 force field [59] using the TIP4P solvent model. The charges were neutralized by adding $Na^+/Cl^-$ ions, and the equivalent of 150 mM NaCl was introduced to the system. Prior to the production simulations, a standard relaxation protocol was applied. MD simulations were run for 1000 ns at 310 K under NPT conditions. Trajectory data were recorded every 1 ns (1000 frames per system; Supplementary Fig. S1). The structural and dynamic properties of each of the ten subunits within each system were analyzed independently, utilizing tools included in *Maestro*.

### 4.10. Other software

ADME properties related to solubility were calculated with QikProp (Schrödinger, LLC, New York, NY, 2025). Molecular figures were prepared with UCSF Chimera [60].

## Authors contribution

WR produced the protein, crystallized it, solved the structures, and drafted the manuscript. DC crystallized the protein, wrote part of the manuscript, and edited the text. LHT helped with the protein purification and crystallization for the soaking campaign. GF wrote a part of the manuscript. MR secured the funding, supervised the project, performed

soaking, and edited the manuscript.

## CRediT authorship contribution statement

**Wiktoria Ragin-Oh:** Writing – original draft, Visualization, Validation, Investigation. **Dominika Czerwonka:** Writing – original draft, Investigation. **Linh H. Tran:** Investigation. **Giuseppe Forlani:** Writing – original draft. **Milosz Ruszkowski:** Writing – review & editing, Supervision, Project administration, Methodology, Funding acquisition, Conceptualization.

## Declaration of generative AI and AI-assisted technologies in the writing process

During the preparation of this work, the authors used ChatGPT in order to correct the language of the work and improve readability. After using this tool, the authors reviewed and edited the content as needed and take full responsibility for the content of the publication.

## Funding

National Science Centre (Poland), grant number: 2021/43/B/NZ7/01611.

## Declaration of competing interest

The authors declare that they have no known competing financial interests or personal relationships that could have influenced the work reported in this paper.

## Acknowledgments

The authors are grateful to Manfred Weiss and Jan Wollenhaupt (BESSY, Berlin, Germany) for sharing the F2X-Entry library. The library usage and the beamtime allocation were ensured within the iNext Discovery program, project ID: 25069. The authors are also extremely thankful to Tobias Krojer for the support during the sample transfer and data collection at the BioMAX beamline at MAX IV laboratory (Lund, Sweden). The diffraction data were also collected at beamline P13 operated by EMBL Hamburg at the PETRA III storage ring (DESY, Hamburg, Germany).

## Appendix A. Supplementary data

Supplementary data to this article can be found online at https://doi.org/10.1016/j.bioorg.2025.109024.

## Data availability

The crystal structures for the PYCR1 complexes have been deposited in the Protein Data Bank (PDB, www.rcsb.org) under the following accession codes: PYCR1-D11, 9S02; PYCR1-H9, 9S04; PYCR1-TLA, 9S01; and PYCR1-P1S, 9RZZ. Raw diffraction data, processing files, *E*-maps, and the refined structural models for all structures reported herein are available from the Macromolecular Xtallography Raw Data Repository (MX-RDR; https://mxrdr.icm.edu.pl/): PYCR1-B5, https://doi.org/10.60884/0ZLQND; PYCR1-D2, https://doi.org/10.60884/EIUWD8; PYCR1-D11, https://doi.org/10.60884/NRNGS4; PYCR1-F3, https://doi.org/10.60884/ZKISSR; PYCR1-F4, https://doi.org/10.60884/XBAAAB; PYCR1-G5, https://doi.org/10.60884/XFCP9Z; PYCR1-G9, https://doi.org/10.60884/VKJZQ0; PYCR1-H3, https://doi.org/10.60884/GPGJPK; PYCR1-H4, https://doi.org/10.60884/ZQEZ9G; PYCR1-H9, https://doi.org/10.60884/VLUTJ1; PYCR1-TLA, https://doi.org/10.60884/PVIXQ6; PYCR1-P1S, https://doi.org/10.60884/DSLYQF.

## References

[1] L.A. Vettore, R.L. Westbrook, D.A. Tennant, Proline metabolism and redox; maintaining a balance in health and disease, Amino Acids 53 (12) (2021) 1779–1788, https://doi.org/10.1007/s00726-021-03051-2.
[2] C. D'Aniello, E.J. Patriarca, J.M. Phang, G. Minchiotti, Proline metabolism in tumor growth and metastatic progression, Front. Oncol. 10 (2020) 776, https://doi.org/10.3389/fonc.2020.00776.
[3] J. Guo, X. Cheng, Y. Tian, B. Li, X. Zhang, X. Gao, Y. An, Knockdown of PYCR1 suppressed the malignant phenotype of human hepatocellular carcinoma cells via inhibiting the AKT pathway activation, Reprod. Biol. 21 (3) (2021) 100534, https://doi.org/10.1016/j.repbio.2021.100534.
[4] Y. Xu, W. Zuo, X. Wang, Q. Zhang, X. Gan, N. Tan, W. Jia, J. Liu, Z. Li, B. Zhou, D. Zhao, Z. Xie, Y. Tan, S. Zheng, C. Liu, H. Li, Z. Chen, X. Yang, Z. Huang, Deciphering the effects of PYCR1 on cell function and its associated mechanism in hepatocellular carcinoma, Int. J. Biol. Sci. 17 (9) (2021) 2223–2239, https://doi.org/10.7150/ijbs.58026.
[5] Z. Ding, R.E. Ericksen, Q.Y. Lee, W. Han, Reprogramming of mitochondrial proline metabolism promotes liver tumorigenesis, Amino Acids 53 (12) (2021) 1807–1815, https://doi.org/10.1007/s00726-021-02961-5.
[6] Z. Ding, R.E. Ericksen, N. Escande-Beillard, Q.Y. Lee, A. Loh, S. Denil, M. Steckel, A. Haegebarth, T.S. Wai Ho, P. Chow, H.C. Toh, B. Reversade, S. Gruenewald, W. Han, Metabolic pathway analyses identify proline biosynthesis pathway as a promoter of liver tumorigenesis, J. Hepatol. 72 (4) (2020) 725–735, https://doi.org/10.1016/j.jhep.2019.10.026.
[7] J. Ding, M.L. Kuo, L. Su, L. Xue, F. Luh, H. Zhang, J. Wang, T.G. Lin, K. Zhang, P. Chu, S. Zheng, X. Liu, Y. Yen, Human mitochondrial pyrroline-5-carboxylate reductase 1 promotes invasiveness and impacts survival in breast cancers, Carcinogenesis 38 (5) (2017) 519–531, https://doi.org/10.1093/carcin/bgx022.
[8] B. Cui, B. He, Y. Huang, C. Wang, H. Luo, J. Lu, K. Su, X. Zhang, Y. Luo, Z. Zhao, Y. Yang, Y. Zhang, F. An, H. Wang, E.W. Lam, K.W. Kelley, L. Wang, Q. Liu, F. Peng, Pyrroline-5-carboxylate reductase 1 reprograms proline metabolism to drive breast cancer stemness under psychological stress, Cell Death Dis. 14 (10) (2023) 682, https://doi.org/10.1038/s41419-023-06200-5.
[9] A. Shenoy, N. Belugali Nataraj, G. Perry, F. Loayza Puch, R. Nagel, I. Marin, N. Balint, N. Bossel, A. Pavlovsky, I. Barshack, B. Kaufman, R. Agami, Y. Yarden, M. Dadiani, T. Geiger, Proteomic patterns associated with response to breast cancer neoadjuvant treatment, Mol. Syst. Biol. 16 (9) (2020) e9443, https://doi.org/10.15252/msb.20209443.
[10] T. Zeng, L. Zhu, M. Liao, W. Zhuo, S. Yang, W. Wu, D. Wang, Knockdown of PYCR1 inhibits cell proliferation and colony formation via cell cycle arrest and apoptosis in prostate cancer, Med. Oncol. 34 (2) (2017) 27, https://doi.org/10.1007/s12032-016-0870-5.
[11] T. Ernst, M. Hergenhahn, M. Kenzelmann, C.D. Cohen, M. Bonrouhi, A. Weninger, R. Klaren, E.F. Grone, M. Wiesel, C. Gudemann, J. Kuster, W. Schott, G. Staehler, M. Kretzler, M. Hollstein, H.J. Grone, Decrease and gain of gene expression are equally discriminatory markers for prostate carcinoma: a gene expression analysis on total and microdissected prostate tissue, Am. J. Pathol. 160 (6) (2002) 2169–2180, https://doi.org/10.1016/S0002-9440(10)61165-0.
[12] Y. Ye, Y. Wu, J. Wang, Pyrroline-5-carboxylate reductase 1 promotes cell proliferation via inhibiting apoptosis in human malignant melanoma, Cancer Manag. Res. 10 (2018) 6399–6407, https://doi.org/10.2147/CMAR.S166711.
[13] Y. Li, J. Xu, P. Bao, Z. Wei, L. Pan, J. Zhou, W. Wang, Survival and clinicopathological significance of PYCR1 expression in cancer: a meta-analysis, Front. Oncol. 12 (2022) 985613, https://doi.org/10.3389/fonc.2022.985613.
[14] S. Xiao, S. Li, Z. Yuan, L. Zhou, Pyrroline-5-carboxylate reductase 1 (PYCR1) upregulation contributes to gastric cancer progression and indicates poor survival outcome, Ann. Transl. Med. 8 (15) (2020) 937, https://doi.org/10.21037/atm-19-4402.
[15] S. Sang, C. Zhang, J. Shan, Pyrroline-5-carboxylate reductase 1 accelerates the migration and invasion of nonsmall cell lung Cancer in vitro, Cancer Biother. Radiopharm. 34 (6) (2019) 380–387, https://doi.org/10.1089/cbr.2019.2782.
[16] Z. Li, Y. Jiang, J. Liu, H. Fu, Q. Yang, W. Song, Y. Li, Exosomes from PYCR1 knockdown bone marrow mesenchymal stem inhibits aerobic glycolysis and the growth of bladder cancer cells via regulation of the EGFR/PI3K/AKT pathway, Int. J. Oncol. 63 (1) (2023), https://doi.org/10.3892/ijo.2023.5532.
[17] I. Elia, D. Broekaert, S. Christen, R. Boon, E. Radaelli, M.F. Orth, C. Verfaillie, T.G. P. Grunewald, S.M. Fendt, Proline metabolism supports metastasis formation and could be inhibited to selectively target metastasizing cancer cells, Nat. Commun. 8 (2017) 15267, https://doi.org/10.1038/ncomms15267.
[18] J.M. Phang, Proline metabolism in cell regulation and Cancer biology: recent advances and hypotheses, Antioxid. Redox Signal. 30 (4) (2019) 635–649, https://doi.org/10.1089/ars.2017.7350.
[19] F. Loayza-Puch, K. Rooijers, L.C. Buil, J. Zijlstra, J.F. Oude Vrielink, R. Lopes, A. P. Ugalde, P. van Breugel, I. Hofland, J. Wesseling, O. van Tellingen, A. Bex, R. Agami, Tumour-specific proline vulnerability uncovered by differential ribosome codon reading, Nature 530 (7591) (2016) 490–494, https://doi.org/10.1038/nature16982.
[20] C. D'Aniello, A. Fico, L. Casalino, O. Guardiola, G. Di Napoli, F. Cermola, D. De Cesare, R. Tate, G. Cobellis, E.J. Patriarca, G. Minchiotti, A novel autoregulatory loop between the Gcn2-Atf4 pathway and l-proline metabolism controls stem cell identity, Cell Death Differ. 22 (7) (2015) 1234, https://doi.org/10.1038/cdd.2015.64.
[21] E.J. Kay, K. Paterson, C. Riera-Domingo, D. Sumpton, J.H.M. Dabritz, S. Tardito, C. Boldrini, J.R. Hernandez-Fernaud, D. Athineos, S. Dhayade, E. Stepanova, E. Gjerga, L.J. Neilson, S. Lilla, A. Hedley, G. Koulouras, G. McGregor, C. Jamieson,

R.M. Johnson, M. Park, K. Kirschner, C. Miller, J.J. Kamphorst, F. Loayza-Puch, J. Saez-Rodriguez, M. Mazzone, K. Blyth, M. Zagnoni, S. Zanivan, Cancer-associated fibroblasts require proline synthesis by PYCR1 for the deposition of pro-tumorigenic extracellular matrix, Nat. Metab. 4 (6) (2022) 693–710, https://doi.org/10.1038/s42255-022-00582-0.

[22] R.L. Westbrook, E. Bridges, J. Roberts, C. Escribano-Gonzalez, K.L. Eales, L. A. Vettore, P.D. Walker, E. Vera-Siguenza, H. Rana, F. Cuozzo, K.L. Eskla, H. Vellama, A. Shaaban, C. Nixon, H. Luuk, G.G. Lavery, D.J. Hodson, A.L. Harris, D.A. Tennant, Proline synthesis through PYCR1 is required to support cancer cell proliferation and survival in oxygen-limiting conditions, Cell Rep. 38 (5) (2022) 110320, https://doi.org/10.1016/j.celrep.2022.110320.

[23] K.E.R. Hollinshead, H. Munford, K.L. Eales, C. Bardella, C. Li, C. Escribano-Gonzalez, A. Thakker, Y. Nonnenmacher, K. Kluckova, M. Jeeves, R. Murren, F. Cuozzo, D. Ye, G. Laurenti, W. Zhu, K. Hiller, D.J. Hodson, W. Hua, I. P. Tomlinson, C. Ludwig, Y. Mao, D.A. Tennant, Oncogenic IDH1 mutations promote enhanced proline synthesis through PYCR1 to support the maintenance of mitochondrial redox homeostasis, Cell Rep. 22 (12) (2018) 3107–3114, https://doi.org/10.1016/j.celrep.2018.02.084.

[24] K.W. Ryu, T.S. Fung, D.C. Baker, M. Saoi, J. Park, C.A. Febres-Aldana, R.G. Aly, R. Cui, A. Sharma, Y. Fu, O.L. Jones, X. Cai, H.A. Pasolli, J.R. Cross, C.M. Rudin, C. B. Thompson, Cellular ATP demand creates metabolically distinct subpopulations of mitochondria, Nature 635 (8039) (2024) 746–754, https://doi.org/10.1038/s41586-024-08146-w.

[25] C.H. Hagedorn, J.M. Phang, Catalytic transfer of hydride ions from NADPH to oxygen by the interconversions of proline and delta 1-pyrroline-5-carboxylate, Arch. Biochem. Biophys. 248 (1) (1986) 166–174, https://doi.org/10.1016/0003-9861(86)90413-3.

[26] J. De Ingeniis, B. Ratnikov, A.D. Richardson, D.A. Scott, P. Aza-Blanc, S.K. De, M. Kazanov, M. Pellecchia, Z. Ronai, A.L. Osterman, J.W. Smith, Functional specialization in proline biosynthesis of melanoma, PLoS ONE 7 (9) (2012) e45190, https://doi.org/10.1371/journal.pone.0045190.

[27] J.M. Phang, W. Liu, O. Zabirnyk, Proline metabolism and microenvironmental stress, Annu. Rev. Nutr. 30 (2010) 441–463, https://doi.org/10.1146/annurev.nutr.012809.104638.

[28] J.J. Tanner, S.M. Fendt, D.F. Becker, The proline cycle as a potential Cancer therapy target, Biochemistry 57 (25) (2018) 3433–3444, https://doi.org/10.1021/acs.biochem.8b00215.

[29] J.M. Phang, S.P. Donald, J. Pandhare, Y. Liu, The metabolism of proline, a stress substrate, modulates carcinogenic pathways, Amino Acids 35 (4) (2008) 681–690, https://doi.org/10.1007/s00726-008-0063-4.

[30] W. Liu, J.M. Phang, Proline dehydrogenase (oxidase) in cancer, Biofactors 38 (6) (2012) 398–406, https://doi.org/10.1002/biof.1036.

[31] E.M. Christensen, A.N. Bogner, A. Vandekeere, G.S. Tam, S.M. Patel, D.F. Becker, S. M. Fendt, J.J. Tanner, In crystallo screening for proline analog inhibitors of the proline cycle enzyme PYCR1, J. Biol. Chem. 295 (52) (2020) 18316–18327, https://doi.org/10.1074/jbc.RA120.016106.

[32] K.R. Meeks, J. Ji, M.V. Protopopov, O.O. Tarkhanova, Y.S. Moroz, J.J. Tanner, Novel fragment inhibitors of PYCR1 from docking-guided X-ray crystallography, J. Chem. Inf. Model. 64 (5) (2024) 1704–1718, https://doi.org/10.1021/acs.jcim.3c01879.

[33] K. Milne, J. Sun, E.A. Zaal, J. Mowat, P.H.N. Celie, A. Fish, C.R. Berkers, G. Forlani, F. Loayza-Puch, C. Jamieson, R. Agami, A fragment-like approach to PYCR1 inhibition, Bioorg. Med. Chem. Lett. 29 (18) (2019) 2626–2631, https://doi.org/10.1016/j.bmcl.2019.07.047.

[34] T.N. Raju, The Nobel chronicles. 1988: James Whyte Black, (b 1924), Gertrude Elion (1918–99), and George H Hitchings (1905–98), Lancet 355 (9208) (2000) 1022, https://doi.org/10.1016/s0140-6736(05)74775-9.

[35] H. Chen, J. Wu, Y. Gao, H. Chen, J. Zhou, Scaffold repurposing of old drugs towards new cancer drug discovery, Curr. Top. Med. Chem. 16 (19) (2016) 2107–2114.

[36] G. Forlani, G. Sabbioni, D. Ragno, D. Petrollino, M. Borgatti, Phenyl-substituted aminomethylene-bisphosphonates inhibit human P5C reductase and show antiproliferative activity against proline-hyperproducing tumour cells, J. Enzyme Inhib. Med. Chem. 36 (1) (2021) 1248–1257, https://doi.org/10.1080/14756366.2021.1919890.

[37] G. Forlani, Effects of substituent and scaffold changes on the inhibition of human P5C reductase by phenyl-substituted Aminomethylene bisphosphonates, Chemistry-Basel 7 (2) (2025) 30, https://doi.org/10.3390/chemistry7020030.

[38] E.M. Christensen, S.M. Patel, D.A. Korasick, A.C. Campbell, K.L. Krause, D. F. Becker, J.J. Tanner, Resolving the cofactor-binding site in the proline biosynthetic enzyme human pyrroline-5-carboxylate reductase 1, J. Biol. Chem. 292 (17) (2017) 7233–7243, https://doi.org/10.1074/jbc.M117.780288.

[39] F. Gorrec, The MORPHEUS protein crystallization screen, J. Appl. Crystallogr. 42 (Pt 6) (2009) 1035–1042, https://doi.org/10.1107/S0021889809042022.

[40] J. Wollenhaupt, A. Metz, T. Barthel, G.M.A. Lima, A. Heine, U. Mueller, G. Klebe, M.S. Weiss, F2X-universal and F2X-entry: structurally diverse compound libraries for crystallographic fragment screening, Structure 28 (6) (2020), https://doi.org/10.1016/j.str.2020.04.019, 694-+.

[41] S.K. Burley, H.M. Berman, C. Bhikadiya, C.X. Bi, L. Chen, L. Di Costanzo, C. Christie, J.M. Duarte, S. Dutta, Z.K. Feng, S. Ghosh, D.S. Goodsell, R.K. Green, V. Guranovic, D. Guzenko, B.P. Hudson, Y.H. Liang, R. Lowe, E. Peisach, I. Periskova, C. Randle, A. Rose, M. Sekharan, C.H. Shao, Y.P. Tao, Y. Valasatava, M. Voigt, J. Westbrook, J. Young, C. Zardecki, M. Zhuravleva, G. Kurisu, H. Nakamura, Y. Kengaku, H. Cho, J. Sato, J.Y. Kim, Y. Ikegawa, A. Nakagawa, R. Yamashita, T. Kudou, G.J. Bekker, H. Suzuki, T. Iwata, M. Yokochi, N. Kobayashi, T. Fujiwara, S. Velankar, G.J. Kleywegt, S. Anyango, D. R. Armstrong, J.M. Berrisford, M.J. Conroy, J.M. Dana, M. Deshpande, P. Gane, R. Gáborová, D. Gupta, A. Gutmanas, J. Koca, L. Mak, S. Mir, A. Mukhopadhyay, N. Nadzirin, S. Nair, A. Patwardhan, T. Paysan-Lafosse, L. Pravda, O. Salih, D. Sehnal, M. Varadi, R. Vareková, J.L. Markley, J.C. Hoch, P.R. Romero, K. Baskaran, D. Maziuk, E.L. Ulrich, J.R. Wedell, H.Y. Yao, M. Livny, Y.E. Ioannidis, wwPDB consortium Japan, Protein Data Bank: the single global archive for 3D macromolecular structure data, Nucleic Acids Res. 47 (D1) (2019) D520–D528, https://doi.org/10.1093/nar/gky949.

[42] N.M. Pearce, T. Krojer, A.R. Bradley, P. Collins, R.P. Nowak, R. Talon, B. D. Marsden, S. Kelm, J. Shi, C.M. Deane, F. von Delft, A multi-crystal method for extracting obscured crystallographic states from conventionally uninterpretable electron density, Nat. Commun. 8 (2017) 15123, https://doi.org/10.1038/ncomms15123.

[43] I.W. Davis, A. Leaver-Fay, V.B. Chen, J.N. Block, G.J. Kapral, X. Wang, L. W. Murray, W.B. Arendall, J. Snoeyink, J.S. Richardson, D.C. Richardson, MolProbity: all-atom contacts and structure validation for proteins and nucleic acids, Nucleic Acids Res. 35 (2007) W375–W383, https://doi.org/10.1093/nar/gkm216.

[44] G. Forlani, S. Giberti, L. Berlicki, D. Petrollino, P. Kafarski, Plant P5C reductase as a new target for aminomethylenebisphosphonates, J. Agric. Food Chem. 55 (11) (2007) 4340–4347, https://doi.org/10.1021/jf0701032.

[45] S.M. Patel, J. Seravalli, X.W. Liang, J.J. Tanner, D.F. Becker, Disease variants of human A1-pyrroline-5-carboxylate reductase 2 (PYCR2), Arch. Biochem. Biophys. 703 (2021) 108852, https://doi.org/10.1016/j.abb.2021.108852.

[46] K.R. Meeks, A.N. Bogner, J.J. Tanner, Screening a knowledge-based library of low molecular weight compounds against the proline biosynthetic enzyme 1-pyrroline-5-carboxylate 1 (PYCR1), Protein Sci.: Publ. Protein Soc. 33 (7) (2024) e5072, https://doi.org/10.1002/pro.5072.

[47] P. Lassalas, B. Gay, C. Lasfargeas, M.J. James, V. Tran, K.G. Vijayendran, K. R. Brunden, M.C. Kozlowski, C.J. Thomas, A.B. Smith 3rd, D.M. Huryn, C. Ballatore, Structure property relationships of carboxylic acid Isosteres, J. Med. Chem. 59 (7) (2016) 3183–3203, https://doi.org/10.1021/acs.jmedchem.5b01963.

[48] Y. Kim, G. Babnigg, R. Jedrzejczak, W.H. Eschenfeldt, H. Li, N. Maltseva, C. Hatzos-Skintges, M.Y. Gu, M. Makowska-Grzyska, R.Y. Wu, H. An, G. Chhor, A. Joachimiak, High-throughput protein purification and quality assessment for crystallization, Methods 55 (1) (2011) 12–28, https://doi.org/10.1016/j.ymeth.2011.07.010.

[49] H.E. Klock, S.A. Lesley, The polymerase incomplete primer extension (PIPE) method applied to high-throughput cloning and site-directed mutagenesis, Methods Mol. Biol. 498 (2009) 91–103, https://doi.org/10.1007/978-1-59745-196-3_6.

[50] T. Ursby, K. Åhnberg, R. Appio, O. Aurelius, A. Barczyk, A. Bartalesi, M. Bjelcic, F. Bolmsten, Y. Cerenius, R.B. Doak, M. Eguiraun, T. Eriksson, R.J. Friel, I. Gorgisyan, A. Gross, V. Haghighat, F. Hennies, E. Jagudin, B.N. Jensen, T. Jeppsson, M. Kloos, J. Lidon-Simon, G.M.A. de Lima, R. Lizatovic, M. Lundin, A. Milan-Otero, M. Milas, J. Nan, A. Nardella, A. Rosborg, A. Shilova, R. L. Shoeman, F. Siewert, P. Sondhauss, V.O. Talibov, H. Tarawneh, J. Thånell, M. Thunnissen, J. Unge, C. Ward, A. Gonzalez, U. Muellera, BioMAX - the first macromolecular crystallography beamline at MAX IV laboratory, J. Synchrotron Radiat. 27 (2020) 1415–1429, https://doi.org/10.1107/S1600577520008723.

[51] M. Cianci, G. Bourenkov, G. Pompidor, I. Karpics, J. Kallio, I. Bento, M. Roessle, F. Cipriani, S. Fiedler, T.R. Schneider, P13, the EMBL macromolecular crystallography beamline at the low-emittance PETRA III ring for high- and low-energy phasing with variable beam focusing, J. Synchrotron Radiat. 24 (Pt 1) (2017) 323–332, https://doi.org/10.1107/S1600577516016465.

[52] W. Kabsch, Xds, Acta Crystallogr. D 66 (Pt 2) (2010) 125–132, https://doi.org/10.1107/S0907444909047337.

[53] M. Wojdyr, R. Keegan, G. Winter, A. Ashton, DIMPLE - a pipeline for the rapid generation of difference maps from protein crystals with putatively bound ligands, Acta Crystallogr. A 69 (2013) S299, https://doi.org/10.1107/S0108767313097419.

[54] J. Agirre, M. Atanasova, H. Bagdonas, C.B. Ballard, A. Baslé, J. Beilsten-Edmands, R.J. Borges, D.G. Brown, J.J. Burgos-Mármol, J.M. Berrisford, P.S. Bond, I. Caballero, L. Catapano, G. Chojnowski, A.G. Cook, K.D. Cowtan, T.I. Croll, J.É. Debreczeni, N.E. Devenish, E.J. Dodson, T.R. Drevon, P. Emsley, G. Evans, P. R. Evans, M. Fando, J. Foadi, L. Fuentes-Montero, E.F. Garman, M. Gerstel, R. J. Gildea, K. Hatti, M.L. Hekkelman, P. Heuser, S.W. Hoh, M.A. Hough, H. T. Jenkins, E. Jiménez, R.P. Joosten, R.M. Keegan, N. Keep, E.B. Krissinel, P. Kolenko, O. Kovalevskiy, V.S. Lamzin, D.M. Lawson, A.A. Lebedev, A.G. W. Leslie, B. Lohkamp, F. Long, M. Maly, A.J. McCoy, S.J. McNicholas, A. Medina, C. Millán, J.W. Murray, G.N. Murshudov, R.A. Nicholls, M.E.M. Noble, R. Oeffner, N.S. Pannu, J.M. Parkhurst, N. Pearce, J. Pereira, A. Perrakis, H.R. Powell, R. J. Read, D.J. Rigden, W. Rochira, M. Sammito, F.S. Rodríguez, G.M. Sheldrick, K. L. Shelley, F. Simkovic, A.J. Simpkin, P. Skubak, E. Sobolev, R.A. Steiner, K. Stevenson, I. Tews, J.M.H. Thomas, A. Thorn, J.T. Valls, V. Uski, I. Usón, A. Vagin, S. Velankar, M. Vollmar, H. Walden, D. Waterman, K.S. Wilson, M. D. Winn, G. Winter, M. Wojdyr, K. Yamashita, The CCP4 suite: integrative software for macromolecular crystallography, Acta Crystallogr. D 79 (2023) 449–461, https://doi.org/10.1107/S2059798323003595.

[55] P. Emsley, B. Lohkamp, W.G. Scott, K. Cowtan, Features and development of coot, Acta Crystallogr. D Biol. Crystallogr. 66 (Pt 4) (2010) 486–501, https://doi.org/10.1107/S0907444910007493.

[56] P.V. Afonine, R.W. Grosse-Kunstleve, N. Echols, J.J. Headd, N.W. Moriarty, M. Mustyakimov, T.C. Terwilliger, A. Urzhumtsev, P.H. Zwart, P.D. Adams, Towards automated crystallographic structure refinement with phenix.Refine, Acta

Crystallogr. D Biol. Crystallogr. 68 (2012) 352–367, https://doi.org/10.1107/S0907444912001308.

[57] I. Williams, L. Frank, Improved chemical synthesis and enzymatic assay of Delta-1-Pyrroline-5-carboxylic acid, Anal. Biochem. 64 (1) (1975) 85–97, https://doi.org/10.1016/0003-2697(75)90408-X.

[58] K.J. Bowers, E. Chow, H. Xu, R.O. Dror, M.P. Eastwood, B.A. Gregersen, J. L. Klepeis, I. Kolossvary, M.A. Moraes, F.D. Sacerdoti, J.K. Salmon, Y. Shan, D. E. Shaw, Scalable Algorithms for Molecular Dynamics Simulations on Commodity Clusters, Proceedings of the ACM/IEEE Conference on Supercomputing (SC06), Tampa, Florida, USA, 2006.

[59] C. Lu, C.J. Wu, D. Ghoreishi, W. Chen, L.L. Wang, W. Damm, G.A. Ross, M. K. Dahlgren, E. Russell, C.D. Von Bargen, R. Abel, R.A. Friesner, E.D. Harder, OPLS4: improving force field accuracy on challenging regimes of chemical space, J. Chem. Theory Comput. 17 (7) (2021) 4291–4300, https://doi.org/10.1021/acs.jctc.1c00302.

[60] E.F. Pettersen, T.D. Goddard, C.C. Huang, G.S. Couch, D.M. Greenblatt, E.C. Meng, T.E. Ferrin, UCSF chimera - a visualization system for exploratory research and analysis, J. Comput. Chem. 25 (13) (2004) 1605–1612, https://doi.org/10.1002/jcc.20084.